

Cite this: *Chem. Sci.*, 2021, 12, 8803

All publication charges for this article have been paid for by the Royal Society of Chemistry

The inorganic cation-tailored “trapdoor” effect of silicoaluminophosphate zeolite for highly selective CO₂ separation†

Xiaohe Wang,^{‡a} Nana Yan,^{‡b} Miao Xie,^{‡c} Puxu Liu,^d Pu Bai,^a Haopeng Su,^a Binyu Wang,^a Yunzheng Wang,^a Libo Li,^{id d} Tao Cheng,^{id c} Peng Guo,^{id *b} Wenfu Yan^{id *a} and Jihong Yu^{id *ae}

Functional nanoporous materials are widely explored for CO₂ separation, in particular, small-pore aluminosilicate zeolites having a “trapdoor” effect. Such an effect allows the specific adsorbate to push away the sited cations inside the window followed by exclusive admission to the zeolite pores, which is more advantageous for highly selective CO₂ separation. Herein, we demonstrated that the protonated organic structure-directing agent in the small-pore silicoaluminophosphate (SAPO) RHO zeolite can be directly exchanged with Na⁺, K⁺, or Cs⁺ and that the Na⁺ form of SAPO-RHO exhibited unprecedented separation for CO₂/CH₄, superior to all of the nanoporous materials reported to date. Rietveld refinement revealed that Na⁺ is sited in the center of the single eight-membered ring (s8r), while K⁺ and Cs⁺ are sited in the center of the double 8-rings (d8rs). Theoretical calculations showed that the interaction between Na⁺ and the s8r in SAPO-RHO was stronger than that in aluminosilicate RHO, giving an enhanced “trapdoor” effect and record high selectivity for CO₂ with the separation factor of 2196 for CO₂/CH₄ (0.02/0.98 bar). The separation factor of Na-SAPO-RHO for CO₂/N₂ was 196, which was the top level among zeolitic materials. This work opens a new avenue for gas separation by using diverse silicoaluminophosphate zeolites in terms of the cation-tailored “trapdoor” effect.

Received 1st February 2021

Accepted 13th May 2021

DOI: 10.1039/d1sc00619c

rsc.li/chemical-science

Introduction

The CO₂ concentration in the atmosphere has increased rapidly in recent decades due to the dramatic increase of emissions from industries and power plants, which is believed to have significant influence on global warming.¹ In CO₂ capture and sequestration (CCS), two important issues are the separation of CO₂ from post-combustion (CO₂/N₂) and natural gas mixtures

(CO₂/CH₄).² Industrially, the separation of CO₂/CH₄ and CO₂/N₂ is mainly based on the strong chemical adsorption of amine solutions towards CO₂, which has the drawbacks of complicated operation, strong corrosiveness to equipment, high energy consumption for regeneration, and easy deactivation. Hence, the low-cost and high-efficiency capture and separation of CO₂ has always been highly desired.^{2a,3}

Compared to chemical adsorption, weak physical adsorption based processes for the separation of CO₂/CH₄ and CO₂/N₂ have attracted much attention due to the characteristics of clean, simple operation, and low-energy consumption.⁴ Over recent years, a variety of solid porous materials have been investigated for the separation of CO₂/CH₄ and CO₂/N₂,^{2a,c,3b,5} including carbon-based materials,⁶ zeolites,⁷ metal-organic frameworks (MOFs),⁸ N or amine-functionalized solid porous materials,⁹ porous organic solids, *etc.*¹⁰ Taking into account the key factors governing the separation efficiency of CO₂ such as adsorption capacity, selectivity, adsorption/desorption kinetics, and cost, zeolites, in particular, the small-pore zeolites with the “trapdoor” effect, have more advantages over other materials for industrial utilization.^{4a,b}

The “trapdoor” effect of zeolites was first observed in small-pore chabazite (CHA) zeolites that can even perform “size-inverse” separation.¹¹ For chabazite structures with a low Si/Al ratio (<3), K⁺, Rb⁺, or Cs⁺ ions fully occupy 8-ring windows that

^aState Key Laboratory of Inorganic Synthesis and Preparative Chemistry, College of Chemistry, Jilin University, Changchun 130012, China. E-mail: yanw@jlu.edu.cn; jihong@jlu.edu.cn

^bNational Engineering Laboratory for Methanol to Olefins, Dalian National Laboratory for Clean Energy, Dalian Institute of Chemical Physics, Chinese Academy of Sciences, Dalian 116023, China. E-mail: pguo@dicp.ac.cn

^cInstitute of Functional Nano & Soft Materials (FUNSOM), Jiangsu Key Laboratory for Carbon-Based Functional Materials & Devices, Soochow University, Suzhou 215123, China

^dCollege of Chemistry and Chemical Engineering, Shanxi Key Laboratory of Gas Energy Efficient and Clean Utilization, Taiyuan University of Technology, Taiyuan 030024, Shanxi, China

^eInternational Center of Future Science, Jilin University, Changchun 130012, China

† Electronic supplementary information (ESI) available: Details for synthesis, ion-exchange, characterization, and simulation. CCDC 2056929–2056932. For ESI and crystallographic data in CIF or other electronic format see DOI: 10.1039/d1sc00619c

‡ These authors contributed equally to this work.

connect the *cha* cages. Larger CO molecules have a stronger interaction with the cations than smaller N₂ molecules, which induces temporary and reversible cation deviation from the window sites and allows for exclusive admission of CO (0.376 nm) instead of N₂ (0.364 nm). Such separation also gives a high selectivity of 93 for CO₂/CH₄ separation over a large pressure range.¹¹

Among the small-pore zeolites, aluminosilicate Rho (**RHO**) with remarkable structural flexibility was found to have high selectivity for CO₂ in the separation of CO₂ and CH₄.¹² The idealized **RHO** framework (space group: *Im* $\bar{3}$ *m*) is constructed by double 8-rings (*d8rs*) and *lta* cages as the composite building units (CBUs). Each *lta* cage connects with six *d8rs* in six directions in space, while each *d8r* links two *lta* cages, generating a three-dimensional (3D) channel system with 8-ring pore openings (0.36 nm \times 0.36 nm).¹³

Previous studies show that the hydrated cation form and the dehydrated proton form of zeolite Rho have the highest symmetry of *Im* $\bar{3}$ *m*. The framework of the dehydrated cation form of zeolite Rho undergoes distortions to the non-centrosymmetric *I43m*.¹⁴ During the distortion, the 8-ring geometry is twisted from a circle to an elliptical shape, which reduces the pore aperture and thus adjusts the separation selectivity. Alteration in the type of cations can not only distort the 8-ring geometry but also tune the interaction between the cations and the adsorbates. Notably, the “trapdoor” effect in the dehydrated cation form of zeolite Rho was observed in the selective separation of CO₂/CH₄.^{14c,15} Zeolite Rho showed exceptionally high selectivity for CO₂ in the separation of CO₂/CH₄ and the separation factor was as high as 960, which becomes a benchmark set by zeolites in the separation of CO₂ from CH₄.^{14c,15a}

The SAPO **RHO**-type, denoted as DNL-6 (hereafter denoted as SAPO-**RHO**), was first synthesized by Su *et al.* with diethylamine (DEA) as an organic structure-directing agent (OSDA) in the presence of cetyltrimethylammonium bromide (CTAB) in 2011.¹⁶ Recently, a series of commercialized OSDAs were identified with a novel approach called RSS (Refining, Summarizing, and Searching) for the successful synthesis of SAPO-**RHO**.¹⁷ Considering the remarkable CO₂ selectivity of the cationic forms of aluminosilicate **RHO** attributed to its “trapdoor” effect, we suppose that the cationic forms of SAPO-**RHO** might have a better CO₂ selectivity because the framework of silicoaluminophosphate is more flexible than that of aluminosilicate and the “trapdoor” effect in SAPO could be well tailored. However, in general, the introduction of inorganic cations to the SAPO-**RHO** *via* conventional ion-exchange of cations with the protonated SAPO-**RHO** zeolite will inevitably result in a serious crystallinity loss or even collapse of the framework.^{7c,18}

Herein, we prepared the inorganic cationic form of SAPO-**RHO** zeolites *via* direct ion-exchange of protonated OSDA-containing SAPO-**RHO** with Na⁺, K⁺, or Cs⁺. The Na⁺ form of SAPO-**RHO** (denoted as Na-SAPO-**RHO**) with an optimized cation content showed unprecedented selective separation performance for CO₂ from CH₄ and N₂. The Rietveld refinement and theoretical calculations provided an insight into the intriguing CO₂ separation performance arising from the pronounced “trapdoor” effect. Breakthrough experiments suggested that Na-

SAPO-**RHO** is a promising candidate for CO₂ capture in biogas purification and flue gas separation *via* adsorption-based separation processes.

Results and discussion

The SAPO-**RHO** with the Si/(Si + Al + P) mole ratio of 0.18 was hydrothermally synthesized in the presence of DEA, CTAB, and seeds at 473 K for 48 h. The direct ion-exchange (three cycles) of the Na⁺, K⁺, or Cs⁺ salt solution with the as-synthesized SAPO-**RHO** was performed and the resultant product is denoted as M-SAPO-**RHO** (M = Na, K, and Cs). The exchange degree for Na⁺, K⁺, and Cs⁺ is 87.13, 65.75, and 72.87%, respectively. The detailed information of the synthesis and ion exchange is provided in the ESI† The powder X-ray diffraction (PXRD) (Fig. S1†) and the scanning electron microscopy (SEM) analyses (Fig. S2†) of the as-synthesized SAPO-**RHO** and the ion-exchanged M-SAPO-**RHO**s show that all the SAPO-**RHO**s are well-defined crystals with high crystallinity. Fig. 1a shows the PXRD patterns of the H-SAPO-**RHO** and the calcined M-SAPO-**RHO**s (873 K in air for 4 h). It is worth noting that the diffraction peaks of the calcined M-SAPO-**RHO** samples obviously shift to a high angle compared with those of the H-SAPO-**RHO** and simulated XRD of the idealized **RHO** framework, indicating the constriction of the unit cell and distortion of the framework. The texture properties of the SAPO-**RHO**s were characterized by N₂ adsorption/desorption at 77 K (Table S1†) and the corresponding isotherms are provided in Fig. 1b. Compared with H-SAPO-**RHO**, the N₂ adsorption of M-SAPO-**RHO**s was greatly restricted, as observed in zeolite Rho.^{15a}

The unit cell compositions of the calcined SAPO-**RHO**s given in Table S1† were determined based on energy-dispersive spectroscopy (EDS). The EDS mapping (Fig. S3†) analysis clearly shows that Na⁺, K⁺, or Cs⁺ ions are uniformly distributed in the cavities of the corresponding SAPO-**RHO**.

Considering the fact of that the separation investigations were performed under the dry conditions, we analyzed the structures of dehydrated M-SAPO-**RHO**s *via* the Rietveld refinement against PXRD data. Here, we take Na-SAPO-**RHO** as an example to illustrate the Rietveld refinement process. The initial SAPO-**RHO** structural model was deduced from the idealized **RHO** framework. Because of the alternating distribution of Al and P in the SAPO-**RHO** framework, its space group

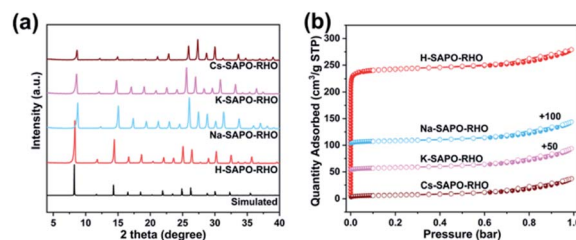


Fig. 1 (a) Simulated XRD pattern of SAPO-**RHO**s and experimental ones of the calcined M-SAPO-**RHO**s; (b) N₂ adsorption/desorption isotherms of the calcined SAPO-**RHO** (H-SAPO-**RHO**) and M-SAPO-**RHO**s (M = Na, K, and Cs) at 77 K.



was reduced to $I432$ (No. 211) from $Im\bar{3}m$ (No. 229). However, it was very challenging to achieve reasonable refinement results for dehydrated Na-**SAPO-RHO** (denoted as de-Na-**SAPO-RHO**) based on the $I432$ space group, since its bond lengths and bond angles deviate heavily from the ideal ones. After scrutinizing the cubic unit cell parameter of de-Na-**SAPO-RHO** ($a = 14.47$ Å), it is quite close to the one of dehydrated distorted zeolite Na-Rho ($a = 14.38$ Å),^{15a} indicating that the crystallographic structure of de-Na-**SAPO-RHO** becomes distorted from the ideal framework

as well. A distorted **SAPO-RHO** structural model (space group $I23$) was constructed based on the dehydrated distorted zeolite Na-Rho ($I\bar{4}3m$), including the initial atomic coordinates for Al, P, and four O atoms in the asymmetric unit. Table S2† shows the space group changes of the H-type and dehydrated cation exchanged zeolite Rho and **SAPO-RHO**.

After profile fitting and optimizing the framework, the scale factor between the simulated PXRD data of the optimized framework and the experimental PXRD data was identified against high angle PXRD data (2θ : 60–120°), where the influence of the extra-framework species (Na^+) in the cavities was negligible. Subsequently, the electron difference density map was calculated by applying the scale factor to the entire range (Fig. 2). Since the guest water molecules were already excluded, the isolated electron density within the cavity indicated the initial positions of the Na^+ ions (inset of Fig. 2). Finally, the Rietveld refinement converged at $R_p = 0.0147$, $R_{wp} = 0.0213$, and $\text{GOF} = 1.526$, which revealed that most of Na^+ ions were located in the elliptical single 8-rings (*s8rs*) and coordinated with framework O atoms (closest Na–O distance: 2.540 Å) and the other fraction (1.92 Na^+ ions per unit cell in average) located close to the single 6-rings (*s6rs*) of *lta* cage as shown in Fig. 3a.

Locations and occupancies of K^+ and Cs^+ ions in the de-K-**SAPO-RHO** and de-Cs-**SAPO-RHO** were determined by utilizing the same method. Unlike Na^+ ions sitting in the center of *s8rs*, K^+ ions in the de-K-**SAPO-RHO** were located at the *d8rs* (center) with the closest K–O distance of 2.713 Å (Fig. 3b). In addition, a small portion of K^+ ions (0.88 per unit cell) settled at the side of *s6rs* of the *lta* cage. For de-Cs-**SAPO-RHO**, Cs^+ ions resided in

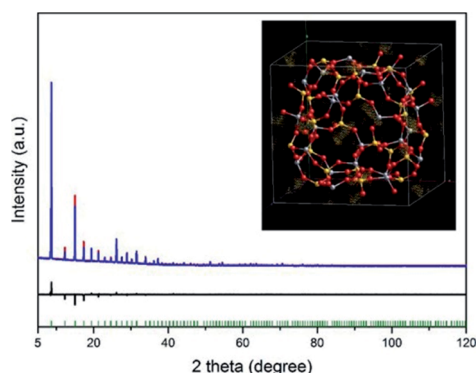


Fig. 2 Plots for locating the Na^+ ions in the de-Na-**SAPO-RHO** by applying the appropriate scale factor to the whole pattern. The inset is the difference electron density map to locate initial positions of Na^+ through Rietveld refinement. The observed, calculated, and difference curves are in blue, red, and black, respectively. The vertical bars indicate the positions of the Bragg peaks ($\lambda = 1.5406$ Å).

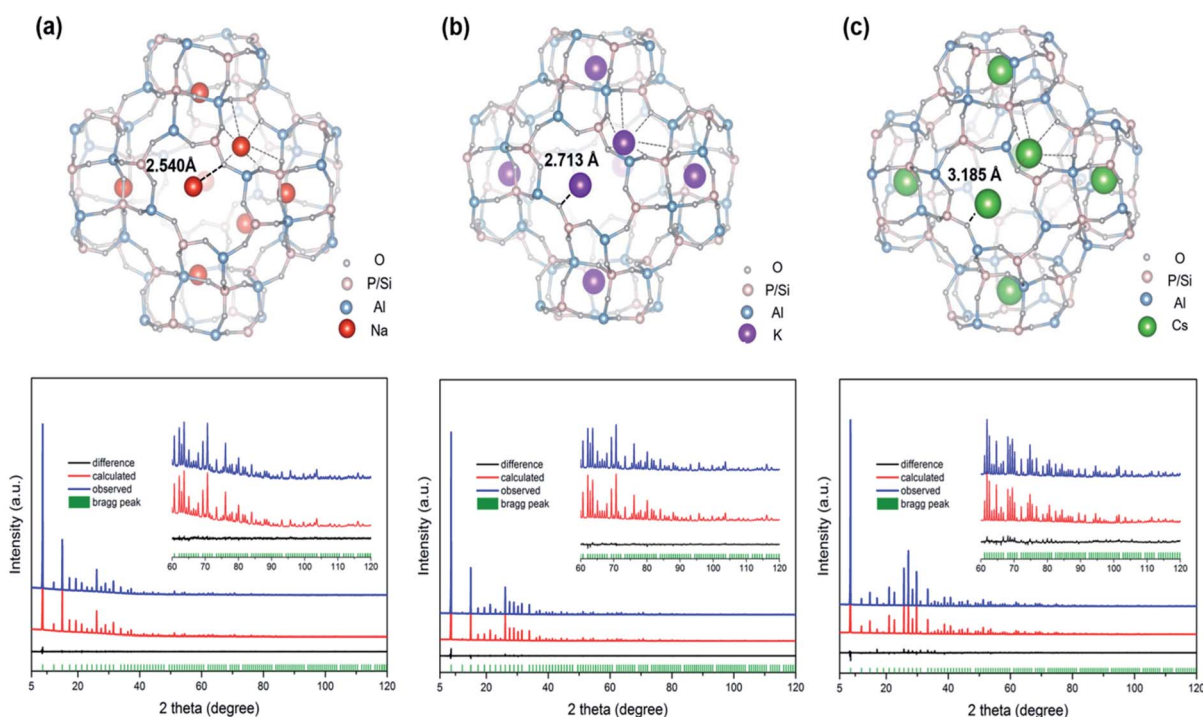


Fig. 3 Crystallographic structures of (a) de-Na-**SAPO-RHO**, (b) de-K-**SAPO-RHO**, and (c) de-Cs-**SAPO-RHO** and their corresponding final Rietveld refinement plots. The observed, calculated, and difference curves are in blue, red, and black, respectively. The vertical bars indicate the positions of the Bragg peaks ($\lambda = 1.5406$ Å).



the center of *d8rs* (closest Cs–O distance: 3.185 Å), while a few Cs⁺ ions (0.6 per unit cell) were close to the center of *s6r* (Fig. 3c). It is worth noting that cations transfer from *s8r* to *d8r* with the increase of the atomic number of the alkaline metal (Na < K < Cs), resulting from a gradually prolonged cation–O bond distance. The detailed structural data for all the SAPO-RHOs are given in Tables S3 and S4.†

To further investigate the structural distortion in cation exchanged SAPO-RHO, a control sample of hydrated Cs-SAPO-RHO was measured. It is worth noting that the unit cell dimensions of the hydrated Cs-SAPO-RHO are the same as the dehydrated one. Hydrated Cs-SAPO-RHO still possesses the space group of *I23* instead of *I432*. It is distinct from the metal exchanged zeolite Rho whose structural distortion only occurred in the process of dehydration. Therefore, it can be clearly concluded that the distortion of the framework of SAPO-RHO is caused solely by the cations of Na⁺, K⁺, or Cs⁺.

The separation performance of the dehydrated H-SAPO-RHOs and M-SAPO-RHOs (M = Na, K, and Cs) were first evaluated by the pure-component equilibrium adsorption isotherms for CO₂, N₂, and CH₄ at 273 K (Fig. S4†), 298 K (Fig. 4a–c), and 313 K (Fig. S4†) between 0 and 1 bar. The results in Fig. 4 and S4† show that all M-SAPO-RHOs have a higher uptake for CO₂ than for CH₄ and N₂, and the uptake of all gases decreases with the increase of temperature. The CO₂ uptake at 298 K and 1 bar is in the order of H-SAPO-RHO (4.41 mmol g^{−1}) > Na-SAPO-RHO (3.53 mmol g^{−1}) > K-SAPO-RHO (0.87 mmol g^{−1}) > Cs-SAPO-RHO (0.45 mmol g^{−1}) (Fig. 4a, Table 1). A higher CO₂ (dynamic diameter of CO₂: 0.33 nm) uptake in the H-SAPO-RHO at 1 bar is attributed to the unblocked 8-ring pore

openings and the small size of protons, leaving more room for CO₂ in the *lta* cage, while it is of interest to note that an appreciable CO₂ uptake (1.21 mmol g^{−1} at 0.02 bar) is observed in the Na-SAPO-RHO although six Na⁺ ions per unit cell occupy the elliptical *s8r* pore openings. It results from the fact that CO₂ with strong quadrupole moment can interact strongly with Na⁺ ions and push them away instantaneously from the center of the *s8rs* to allow the CO₂ molecules to pass through, as observed in the “trapdoor” effect.^{11,14c,15a,19} In addition, an abrupt increase of CO₂ uptake on K-SAPO-RHO above 0.2 bar is observed. Such a shape of the isotherm of CO₂ has been also observed in Na form of MER zeolite with 8MR window, which is attributed to the structural flexibility of the elliptical 8MR window in MER zeolite.²⁰

For CH₄ and N₂, however, the adsorption on Na-SAPO-RHO is very limited (0.027 mmol g^{−1} at 0.98 bar for CH₄ and 0.070 mmol g^{−1} at 0.85 bar for N₂), which might result from the fact that (1) their dynamic diameters (CH₄: 0.38 nm, N₂: 0.36 nm) are larger than effective pore openings; (2) their weaker interactions with Na⁺ ions are insufficient to push the Na⁺ ions away from the center of the *s8rs* to allow the CH₄ and N₂ molecules to pass, *i.e.*, the “trapdoor” remains shut. Notice that the gradual increase of the N₂ uptake on Na-SAPO-RHO with increase of pressure is observed as with H-SAPO-RHO (Fig. 4c) and the H form RHO zeolite.²¹ Elemental analysis shows that the exchange degree of Na⁺ in Na-SAPO-RHO is *ca.* 87.13%, leaving 12.87% of H⁺ balancing the negative charge of the framework of SAPO-RHO. Thus, the gradual increase of the N₂ uptake in Na-SAPO-RHO can be attributed to the existence of H⁺.

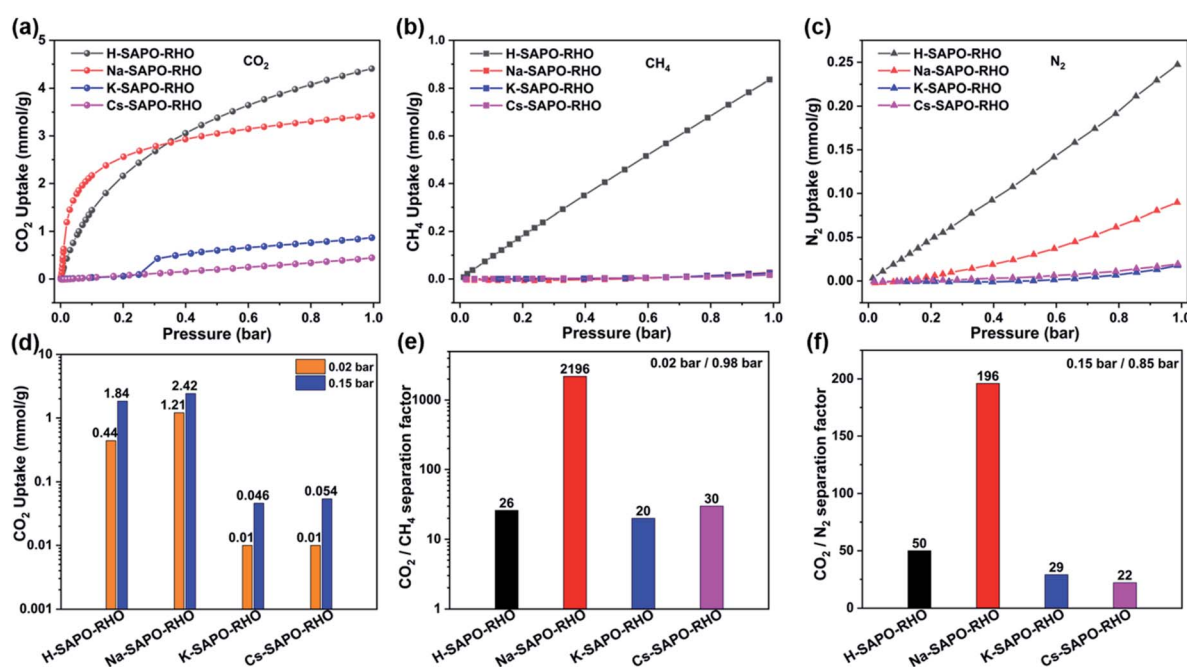


Fig. 4 Comparison of the (a) CO₂, (b) CH₄, and (c) N₂ adsorption isotherms of all SAPO-RHOs at 298 K between 0 and 1 bar; (d) comparison of the CO₂ uptake for all the SAPO-RHOs under 0.02 and 0.15 bar at 298 K respectively; (e) CO₂/CH₄ separation factors at 0.02/0.98 bar and (f) CO₂/N₂ separation factors at 0.15/0.85 bar at 298 K for all the SAPO-RHOs.



Table 1 Comparisons of equilibrium CO₂ uptake and selectivity on various zeolites and SAPOs

Material	CO ₂ uptake [mmol g ⁻¹]		CH ₄ uptake [mmol g ⁻¹]		N ₂ uptake [mmol g ⁻¹]	$\alpha(\text{CO}_2/\text{CH}_4)$ (0.02/0.98 bar)	$\alpha(\text{CO}_2/\text{N}_2)$ (0.15/0.85 bar)	Ref.
	0.02 bar	0.15 bar	1.0 bar	0.98 bar	0.85 bar			
H-SAPO-RHO ^a	0.44	1.84	4.41	0.83	0.210	26	50	This work
Na-SAPO-RHO^a	1.21	2.42	3.53	0.027	0.070	2196	196	This work
K-SAPO-RHO ^a	0.01	0.046	0.87	0.024	0.010	20	29	This work
Cs-SAPO-RHO ^a	0.01	0.054	0.45	0.017	0.014	30	22	This work
Na-1-SAPO-RHO ^a	0.81	2.04	3.43	0.090	0.116	441	105	This work
Na-2-SAPO-RHO ^a	0.71	2.28	3.38	0.042	0.089	828	145	This work
Na-4-SAPO-RHO ^a	0.60	1.82	3.08	0	0	∞	∞	This work
H-SAPO-RHO ^a	0.49	1.95	4.60	0.38	0.23	63	48	24
SAPO-34 ^b	0.24	1.20	3.26	0.65	—	20	—	25
Na-SAPO-34 ^b	0.89	2.10	3.40	0.62	0.26	75	44	25
SAPO-17 ^c	0.29	1.29	3.27	—	0.31	—	23	26
SAPO-35 ^c	0.29	1.87	3.68	—	0.32	—	33	26
SAPO-56 ^c	0.76	2.87	5.44	—	0.39	—	42	26
Na-RHO ^a	2.06	3.30	4.23	0.11	—	960	—	15a
Na-CHA ^a	2.64	3.95	4.70	1.60	0.60	81	37	27
Na-KFI ^d	—	3.40	—	—	0.27	—	71	28
Na-X ^a	2.00	3.17	5.00	0.67	0.23	147	78	29
Na-MER ^a	1.50	2.50	3.80	0.32	—	229	—	30
K-MER ^a	1.93	2.93	3.57	0.052	—	1818	—	30
NaKA (K = 17%) ^a	1.00	2.30	3.43	—	0.02	—	660	22
Na-A ^a	3.20	3.90	4.80	1.34	0.65	117	34	31
Mg-MOF-74 ^a	2.30	5.65	8.00	1.11	—	102	—	32
SIFSIX-3-Zn ^a	1.95	2.30	2.55	0.79	0.46	121	28	32a
UTSA-280 ^a	0.48	1.58	2.78	0.10	0.15	235	60	33

^a The adsorption data were measured at 298 K. ^b The adsorption data were measured at 293 K. ^c The adsorption data were measured at 273 K. ^d The adsorption data were measured at 303 K.

Different from the case in Na-SAPO-RHO, when CO₂, CH₄, and N₂ pass through K-SAPO-RHO or Cs-SAPO-RHO, the K⁺ or Cs⁺ ions located in the center of *d8rs* must first move from *d8r* to *s8r*. Since K⁺ or Cs⁺ ions are located at the center of the *d8rs* and coordinate with more framework oxygen atoms compared with Na⁺ ions in the *s8r*, pushing K⁺ or Cs⁺ ions is energetically much more difficult than moving Na⁺ ions. Thus, there is a lower uptake of CO₂ (0.01 mmol g⁻¹ at 0.02 bar for both K-SAPO-RHO and Cs-SAPO-RHO), N₂ (0.010 mmol g⁻¹ for K-SAPO-RHO and 0.014 mmol g⁻¹ for Cs-SAPO-RHO at 0.85 bar), and CH₄ (0.024 mmol g⁻¹ for K-SAPO-RHO and 0.017 mmol g⁻¹ for Cs-SAPO-RHO at 0.98 bar) in the K-SAPO-RHO and Cs-SAPO-RHO than that in the Na-SAPO-RHO over the entire pressure range as expected (Table 1).

To further evaluate the selectivity of the M-SAPO-RHOs in the separation of CO₂/CH₄ and CO₂/N₂, the separation factor α of CO₂/CH₄ (0.02/0.98 bar) and CO₂/N₂ (0.15/0.85 bar) were calculated on the basis of single-component isotherms (Table 1). The separation factor is highly associated with the CO₂/CH₄/N₂ uptake at the operated pressure. As shown in Fig. 4b and c and Table 1, the CH₄ and N₂ uptakes at the pressure range for Na/K/Cs-SAPO-RHO are comparable and extremely low (0.017–0.027 mmol g⁻¹ for CH₄ and 0.010–0.070 mmol g⁻¹ for N₂). The separation factor thus mainly depends on the uptake of CO₂. Fig. 4d shows the CO₂ uptake of Na/K/Cs-SAPO-RHO at low pressure area and the separation factors for CO₂/CH₄ and CO₂/

N₂ are summarized in Fig. 4e and f, respectively. The detailed uptakes for CO₂/CH₄/N₂ in SAPO-RHOs at various pressures and the corresponding values reported in the literature are provided in Table 1.

Significantly, the separation factor of 2196 of Na-SAPO-RHO for CO₂/CH₄ is more than twice that of 960, superior to all of the nanoporous materials reported to date (Table 1). The separation factor of Na-SAPO-RHO for CO₂/N₂ is also as high as 196, which is the top level among zeolitic materials. The unprecedented high separation factor of Na-SAPO-RHO for CO₂/CH₄ and CO₂/N₂ is in fact due to the much lower uptake of CH₄ (0.027 mmol g⁻¹ at 0.98 bar) and N₂ (0.070 mmol g⁻¹ at 0.85 bar) than that in all other nanoporous materials. We also evaluated the uptake rate (*i.e.*, rate of adsorption) of M-SAPO-RHOs. Considering that the adsorption capacity for CH₄ and N₂ was very low, we measured only the rate of adsorption for CO₂. The rate of adsorption curves for H-SAPO-RHO, Na-SAPO-RHO, K-SAPO-RHO, and Cs-SAPO-RHO at 298 K and 1.0 bar are provided in Fig. S5.† As shown in Fig. S5,† the rate of adsorption of H-SAPO-RHO and Na-SAPO-RHO is much higher than that of K-SAPO-RHO and Cs-SAPO-RHO, which is attributed to the trapdoor effect caused by different cations.

To estimate the error in selectivity of the Na-SAPO-RHO, we prepared two more batches of the Na-SAPO-RHO (denoted as batches 2 and 3, the original Na-SAPO-RHO is denoted as batch



1) and conducted N_2 adsorption/desorption (isotherms in Fig. S6 and textural properties in Table S5†).

Moreover, the pure component adsorption isotherms of CO_2 , CH_4 , and N_2 for the three batches of Na-SAPO-RHO were also measured (Fig. S7a–c†) and the average uptake of CO_2 , CH_4 , and N_2 with error bars plotted is shown in Fig. S7d–f.† As shown in Fig. S7,† the adsorption capacities of the three batches of Na-SAPO-RHO for CO_2 , CH_4 , and N_2 are very similar to each other. The separation factors of the three batches of Na-SAPO-RHO for CO_2/CH_4 and CO_2/N_2 were calculated from their adsorption isotherms and plotted as shown in Fig. S8a and b,† respectively, which show that error in selectivity from batch to batch is very little.

To elucidate how the locations of inorganic cations affect the gas separation performance, we carried out the periodic DFT calculations using the Vienna *ab initio* simulation package (VASP 5.4.4). The details of calculations are presented in the ESI.† The results illustrate that N_2 and CH_4 have weaker interactions with inorganic cations in the Na/K/Cs-SAPO-RHO framework than CO_2 as shown in Table S6† and they only interact with inorganic cations locating in the *s6rs*. It is of significance to note that the CO_2 molecules in the Na-SAPO-RHO sample are captured by two Na^+ ions that are distributed in the *s6rs* and *s8rs*, respectively (Fig. S9†). However, it is distinct from the situations observed in K/Cs-SAPO-RHO in which CO_2 interacts with K^+/Cs^+ ions in the *s6rs* solely (Fig. S11†). These results indicate that CO_2 molecules have a stronger interaction with Na-SAPO-RHO than with K/Cs-SAPO-RHO, which well explains a higher uptake of CO_2 in Na-SAPO-RHO than in K/Cs-SAPO-RHO at the low pressure.

To gain a deep understanding on the different performance between Na-SAPO-RHO and zeolite Na-Rho, density functional theory (DFT) calculations were conducted based on the cluster modes. As shown in Fig. 5, two neutral $Na_5Al_5Si_{43}O_{72}(OH)_{48}$ and $Na_4Si_4Al_{24}P_{20}O_{72}(OH)_{48}$ clusters cut from zeolite Na-Rho and Na-SAPO-RHO were utilized for the theoretical calculations. The details of calculations are presented in the ESI.† The calculated results show that the energy required to push the Na^+ away from the center of the elliptical *s8rs* of the $Na_5Al_5Si_{43}O_{72}(OH)_{48}$ and $Na_4Si_4Al_{24}P_{20}O_{72}(OH)_{48}$ clusters is 5.30 eV and 6.48 eV,

respectively. The results show that Na^+ ions have a stronger interaction with the SAPO framework than those with the aluminosilicate framework, indicating the enhanced “trapdoor effect” in SAPO-RHO. This means that more energy would be needed for CO_2 , CH_4 , and N_2 to push the Na^+ away from the center of the *s8rs* of Na-SAPO-RHO than from that of zeolite Na-Rho, leading to a lower uptake of $CO_2/CH_4/N_2$ in Na-SAPO-RHO than that in Na-Rho. The strong “trapdoor” effect is especially disadvantageous for CH_4 and N_2 to push Na^+ away because the interaction between Na^+ and CH_4 or N_2 is much weaker than that between Na^+ and CO_2 .^{11,14c,15a,22} This explains why the decrease in the uptake of CH_4 and N_2 in Na-SAPO-RHO is much more pronounced as compared to that of CO_2 , resulting in a higher selectivity for CO_2 .

The above results show that the Na-SAPO-RHO has a better performance than the K- and Cs-SAPO-RHO in the separation of CO_2/CH_4 and CO_2/N_2 . Notice that the exchange degree in Na-SAPO-RHO is 87.13% upon 3 cycles of ion-exchange. To investigate the influence of ion-exchange degree on the separation performance, we further investigated the CO_2 separation of the Na-SAPO-RHOs with the exchange degree of 42.41, 72.64, and 100% upon 1, 2, and 4 cycles of the ion-exchange process. The corresponding products are denoted as Na-1-SAPO-RHO, Na-2-SAPO-RHO, and Na-4-SAPO-RHO, respectively. The compositions and characterization results of the Na-SAPO-RHOs are provided in Table S1, Fig. S12 and S13 in the ESI.†

The single component equilibrium adsorption isotherms of the Na-(1-4)-SAPO-RHOs at 298 K with the pressure up to 1 bar for CO_2 , CH_4 , and N_2 are displayed in Fig. S14a–c,† respectively and the detailed uptakes of all components at various pressures are summarized in Table 1. The CO_2 uptakes of all Na-SAPO-RHOs at 0.02 and 0.15 bar are shown in Fig. S14d.† It is found that the uptake of CH_4 and N_2 gradually decreases with the increase of the ion-exchange degree (CH_4 : 0.090, 0.042, and 0.027 mmol g^{-1} at 0.98 bar for 1, 2, and 3 cycles of exchanged samples, respectively; N_2 : 0.116, 0.089, and 0.070 mmol g^{-1} at 0.85 bar for 1, 2, and 3 cycles of exchanged samples, respectively) and reaches 0 at the 4th cycle of ion-exchange (Table 1 and Fig. S14b and c†). Such results might be attributed to the strong “trapdoor” effect of Na^+ on CH_4 and N_2 and the increased Na^+ blocking of the *s8r* with the increase of exchanged Na^+ . Notice that, the Na-SAPO-RHO (3 cycles of ion-exchange) has the best CO_2 uptake capacity (1.21 mmol g^{-1} at 0.02 bar) and selectivity performance ($\alpha(CO_2/CH_4)$: 2196; $\alpha(CO_2/N_2)$: 196) among the Na-SAPO-RHOs (Table 1 and Fig. S14e and f†). This suggests that the amount and distribution of both Na^+ and H^+ in Na-SAPO-RHO play an important role in determining gas adsorption. In this respect, further understanding is needed on the basis of future detailed structural characterization and theoretical calculations.

The breakthrough experiments of the Na-SAPO-RHO were conducted using binary CO_2/CH_4 (50/50, v/v) and CO_2/N_2 (15/85, v/v) gas mixtures at 298 K and atmospheric pressure (Schematic S1†), mimicking the industrial process conditions of biogas^{2a,23} and flue gas^{2a,34} respectively and the corresponding breakthrough curves are given in Fig. S15.† According to Fig. S15,† CO_2 can be completely separated from CH_4 and N_2 . On the basis

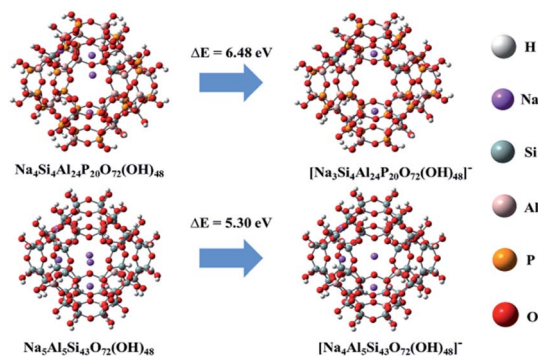


Fig. 5 Molecular structures of two neutral $Na_5Al_5Si_{43}O_{72}(OH)_{48}$ and $Na_4Si_4Al_{24}P_{20}O_{72}(OH)_{48}$ clusters and the binding energy of Na^+ in the center of elliptical *s8rs* in two clusters.



of the breakthrough results, we also calculated the dynamic separation selectivity of the batch 1 of Na-SAPO-RHO for CO₂/CH₄ and CO₂/N₂ (Fig. S16 and S17†). The detailed information for the calculation is included in Section 8 of the ESI.† As shown in Fig. S17,† although the selectivity predicted by the breakthrough curves is slightly lower than that estimated from the multiple pure component adsorption measurements, Na-SAPO-RHO is also highly selective under dynamic conditions, rendering this zeolite potentially useful for selective CO₂ adsorption in practical application.

Conclusions

Silicoaluminophosphate RHO zeolite was hydrothermally synthesized in the presence of diethylamine as an OSDA with the assistance of seeds. Na⁺, K⁺, or Cs⁺ was introduced into the as-prepared SAPO-RHO via direct ion-exchange and complete replacement of protonated diethylamine by Na⁺, while maintaining the zeolite crystallinity, has been successfully achieved upon four cycles of ion-exchange. The structure of ion-exchanged SAPO-RHOs after three cycles is determined by the Rietveld refinement. Structural analyses show that Na⁺ ions are mainly sited in the center of *s8rs*, while the K⁺ and Cs⁺ ions are mainly distributed in the center of *d8rs*. Na⁺ ion-exchanged SAPO-RHO upon three cycles of ion-exchange (Na-SAPO-RHO) exhibits an unprecedented separation factor of 2196 for CO₂/CH₄ and 196 for CO₂/N₂, which is much superior to K⁺ and Cs⁺ exchanged SAPO-RHOs with the same cycles of ion-exchange. Significantly, the Na⁺ form of SAPO-RHO exhibited unprecedented separation for CO₂/CH₄, superior to all the nanoporous materials reported to date. Theoretical calculations show that the interaction between Na⁺ and 8-rings in SAPO-RHO is much stronger than that in aluminosilicate Rho, which leads to a superior separation performance of Na-SAPO-RHO. Complete ion-exchange of Na⁺ in SAPO-RHO further increases the separation factor for CO₂/CH₄ and CO₂/N₂ by further enhancing the “trapdoor” effect. Breakthrough experiments demonstrate that Na-SAPO-RHO can completely separate CO₂ from CH₄ or N₂. These superior features make Na-SAPO-RHO a promising candidate for CO₂ capture in biogas purification and flue gas separation via adsorption-based separation processes. The present work introduces a new promising system based on silicoaluminophosphate zeolites for highly selective gas separation in terms of the cation-tailored “trapdoor” effect.

Author contributions

W. Y. and J. Y. designed and supervised the project; P. B. and Y. W. were involved in the design of the experiments; X. W., H. S., and B. W. performed the experiments; N. Y. and P. G. performed the structural analyses; M. X. and T. C. contributed to the calculations; P. L. and L. L. conducted the adsorption analyses; X. W. wrote the first draft; and W. Y., P. G. and J. Y. deeply revised the manuscript. X. W., N. Y., and M. X. contributed equally to this work.

Conflicts of interest

There are no conflicts to declare.

Acknowledgements

We acknowledge the financial support from the National Natural Science Foundation of China (U1967215, 21835002, and 21621001) and the 111 Project of China (B17020). Dr. Peng Guo acknowledges financial support from the National Natural Science Foundation of China (No. 21972136), CAS Pioneer Hundred Talents Program (Y706071202), Dalian National Laboratory for Clean Energy, (DNL) Cooperation Fund, and Chinese Academy of Sciences (DNL201908). Dr. Nana Yan acknowledges financial support from the CAS Special Research Assistant Program and the scholarship from STOE.

Notes and references

- 1 M. E. Boot-Handford, J. C. Abanades, E. J. Anthony, M. J. Blunt, S. Brandani, N. Mac Dowell, J. R. Fernández, M.-C. Ferrari, R. Gross, J. P. Hallett, R. S. Haszeldine, P. Heptonstall, A. Lyngfelt, Z. Makuch, E. Mangano, R. T. J. Porter, M. Pourkashanian, G. T. Rochelle, N. Shah, J. G. Yao and P. S. Fennell, *Energy Environ. Sci.*, 2014, 7, 130–189.
- 2 (a) Y. S. Bae and R. Q. Snurr, *Angew. Chem., Int. Ed.*, 2011, 50, 11586–11596; (b) H. A. Patel, J. Byun and C. T. Yavuz, *ChemSusChem*, 2017, 10, 1303–1317; (c) M. Pardakhti, T. Jafari, Z. Tobin, B. Dutta, E. Moharreri, N. S. Shemshaki, S. Suib and R. Srivastava, *ACS Appl. Mater. Interfaces*, 2019, 11, 34533–34559.
- 3 (a) H. Yang, Z. Xu, M. Fan, R. Gupta, R. B. Slimane, A. E. Bland and I. Wright, *J. Environ. Sci.*, 2008, 20, 14–27; (b) S. D. Kenarsari, D. Yang, G. Jiang, S. Zhang, J. Wang, A. G. Russell, Q. Wei and M. Fan, *RSC Adv.*, 2013, 3, 22739–22773.
- 4 (a) R. T. Yang, *Gas Separation by Adsorption Processes*, Butterworth, Boston, 1987; (b) R. T. Yang, *Adsorbents: Fundamentals and Applications*, Wiley-Interscience, New York, 2003; (c) R. Ben-Mansour, M. A. Habib, O. E. Bamidele, M. Basha, N. A. A. Qasem, A. Peedikakkal, T. Laoui and M. Ali, *Appl. Energy*, 2016, 161, 225–255; (d) M. Khraisheh, S. Mukherjee, A. Kumar, F. Al Momani, G. Walker and M. J. Zaworotko, *J. Environ. Manage.*, 2020, 255, 109874.
- 5 (a) A. H. Lu and G. P. Hao, *Annu. Rep. Prog. Chem., Sect. A: Inorg. Chem.*, 2013, 109, 484–503; (b) J. Wang, L. Huang, R. Yang, Z. Zhang, J. Wu, Y. Gao, Q. Wang, D. O'Hare and Z. Zhong, *Energy Environ. Sci.*, 2014, 7, 3478–3518; (c) S. Y. Lee and S. J. Park, *J. Ind. Eng. Chem.*, 2015, 23, 1–11; (d) D. D. Zhou, X. W. Zhang, Z. W. Mo, Y. Z. Xu, X. Y. Tian, Y. Li, X. M. Chen and J. P. Zhang, *EnergyChem*, 2019, 1, 100016.
- 6 (a) R. V. Siriwardane, M. S. Shen, E. P. Fisher and J. A. Poston, *Energy Fuels*, 2001, 15, 279–284; (b) A. E. Creamer and B. Gao, *Environ. Sci. Technol.*, 2016, 50, 7276–7289; (c) Z. Zhang,



- Z. P. Cano, D. Luo, H. Dou, A. Yu and Z. Chen, *J. Mater. Chem. A*, 2019, **7**, 20985–21003; (d) S. Wang, Y. Li, S. Dai and D.-E. Jiang, *Angew. Chem., Int. Ed.*, 2020, **59**, 19645–19648.
- 7 (a) K. T. Chue, J. N. Kim, Y. J. Yoo, S. H. Cho and R. T. Yang, *Ind. Eng. Chem. Res.*, 1995, **34**, 591–598; (b) J. Kim, L. C. Lin, J. A. Swisher, M. Haranczyk and B. Smit, *J. Am. Chem. Soc.*, 2012, **134**, 18940–18943; (c) O. Cheung and N. Hedin, *RSC Adv.*, 2014, **4**, 14480–14494; (d) Y.-Y. Wang, Q. Zhang and J.-H. Yu, *Chem. J. Chin. Univ.*, 2020, **41**, 616–622; (e) S.-S. Liu, Y.-C. Chai, N.-J. Guan and L.-D. Li, *Chem. J. Chin. Univ.*, 2021, **42**, 268–288.
- 8 (a) K. Sumida, D. L. Rogow, J. A. Mason, T. M. McDonald, E. D. Bloch, Z. R. Herm, T.-H. Bae and J. R. Long, *Chem. Rev.*, 2012, **112**, 724–781; (b) H. Furukawa, K. E. Cordova, M. O’Keeffe and O. M. Yaghi, *Science*, 2013, **341**, 1230444; (c) C. A. Trickett, A. Helal, B. A. Al-Maythaly, Z. H. Yamani, K. E. Cordova and O. M. Yaghi, *Nat. Rev. Mater.*, 2017, **2**, 17045; (d) Z. Hu, Y. Wang, B. B. Shah and D. Zhao, *Adv. Sustainable Syst.*, 2019, **3**; (e) Y. Jiang, P. Tan, S. Qi, C. Gu, S. Peng, F. Wu, X. Liu and L. Sun, *CCS Chem.*, 2020, **2**, 1659–1668; (f) V. Y. Mao, P. J. Milner, J.-H. Lee, A. C. Forse, E. J. Kim, R. L. Siegelman, C. M. McGuirk, L. B. Porter-Zasada, J. B. Neaton, J. A. Reimer and J. R. Long, *Angew. Chem., Int. Ed.*, 2020, **59**, 19468–19477.
- 9 (a) X. Hu, L. Liu, X. Luo, G. Xiao, E. Shiko, R. Zhang, X. Fan, Y. Zhou, Y. Liu, Z. Zeng and C. Li, *Appl. Energy*, 2020, **260**, 114244; (b) A. M. Varghese and G. N. Karanikolos, *Int. J. Greenhouse Gas Control*, 2020, **96**, 103005.
- 10 (a) J. Wu, F. Xu, S. Li, P. Ma, X. Zhang, Q. Liu, R. Fu and D. Wu, *Adv. Mater.*, 2019, **31**, 1802922; (b) F. Duan, X. Liu, D. Qu, B. Li and L. Wu, *CCS Chem.*, 2020, **2**, 2676–2687.
- 11 J. Shang, G. Li, R. Singh, Q. Gu, K. M. Nairn, T. J. Bastow, N. Medhekar, C. M. Doherty, A. J. Hill, J. Z. Liu and P. A. Webley, *J. Am. Chem. Soc.*, 2012, **134**, 19246–19253.
- 12 M. Palomino, A. Corma, J. L. Jordá, F. Rey and S. Valencia, *Chem. Commun.*, 2012, **48**, 215–217.
- 13 H. E. Robson, D. P. Shoemaker, R. A. Ogilvie and P. C. Manor, in *Molecular Sieves*, American Chemical Society, 1973, ch. 9, vol. 121, pp. 106–115.
- 14 (a) J. B. Parise and D. E. Cox, *J. Phys. Chem.*, 1984, **88**, 1635–1640; (b) J. B. Parise, T. E. Gier, D. R. Corbin, L. Abrams, J. D. Jorgensen and E. Prince, *J. Phys. Chem.*, 1984, **88**, 2303–2307; (c) M. M. Lozinska, J. P. S. Mowat, P. A. Wright, S. P. Thompson, J. L. Jorda, M. Palomino, S. Valencia and F. Rey, *Chem. Mater.*, 2014, **26**, 2052–2061; (d) S. R. G. Balestra, S. Hamad, A. R. Ruiz-Salvador, V. Domínguez-García, P. J. Merkling, D. Dubbeldam and S. Calero, *Chem. Mater.*, 2015, **27**, 5657–5667.
- 15 (a) M. M. Lozinska, E. Mangano, J. P. S. Mowat, A. M. Shepherd, R. F. Howe, S. P. Thompson, J. E. Parker, S. Brandani and P. A. Wright, *J. Am. Chem. Soc.*, 2012, **134**, 17628–17642; (b) M. M. Lozinska, E. Mangano, A. G. Greenaway, R. Fletcher, S. P. Thompson, C. A. Murray, S. Brandani and P. A. Wright, *J. Phys. Chem. C*, 2016, **120**, 19652–19662.
- 16 X. Su, P. Tian, J. Li, Y. Zhang, S. Meng, Y. He, D. Fan and Z. Liu, *Microporous Mesoporous Mater.*, 2011, **144**, 113–119.
- 17 N. Yan, L. Wang, X. Liu, P. Wu, T. Sun, S. Xu, J. Han, P. Guo, P. Tian and Z. Liu, *J. Mater. Chem. A*, 2018, **6**, 24186–24193.
- 18 X. Xiang, M. Yang, B. Gao, Y. Qiao, P. Tian, S. Xu and Z. Liu, *RSC Adv.*, 2016, **6**, 12544–12552.
- 19 T. De Baerdemaeker and D. De Vos, *Nat. Chem.*, 2013, **5**, 89.
- 20 H. J. Choi, D. Jo, J. G. Min and S. B. Hong, *Angew. Chem., Int. Ed.*, 2021, **60**, 4307–4314.
- 21 Q. Ke, T. Sun, X. Wei, Y. Guo, S. Xu and S. Wang, *Chem. Eng. J.*, 2019, **359**, 344–353.
- 22 Q. Liu, A. Mace, Z. Bacsik, J. Sun, A. Laaksonen and N. Hedin, *Chem. Commun.*, 2010, **46**, 4502–4504.
- 23 (a) K. Zhou, S. Chaemchuen and F. Verpoort, *Renewable Sustainable Energy Rev.*, 2017, **79**, 1414–1441; (b) S. Wang, P. Bai, M. Sun, W. Liu, D. Li, W. Wu, W. Yan, J. Shang and J. Yu, *Adv. Sci.*, 2019, **6**, 1901317.
- 24 X. Su, P. Tian, D. Fan, Q. Xia, Y. Yang, S. Xu, L. Zhang, Y. Zhang, D. Wang and Z. Liu, *ChemSusChem*, 2013, **6**, 911–918.
- 25 Y. Luo, H. H. Funke, J. L. Falconer and R. D. Noble, *Ind. Eng. Chem. Res.*, 2016, **55**, 9749–9757.
- 26 O. Cheung, Q. Liu, Z. Bacsik and N. Hedin, *Microporous Mesoporous Mater.*, 2012, **156**, 90–96.
- 27 Y. Guo, T. Sun, Y. Gu, X. Liu, Q. Ke, X. Wei and S. Wang, *Chem.-Asian J.*, 2018, **13**, 3222–3230.
- 28 Q. Liu, T. Pham, M. D. Porosoff and R. F. Lobo, *ChemSusChem*, 2012, **5**, 2237–2242.
- 29 K. S. Walton, M. B. Abney and M. Douglas LeVan, *Microporous Mesoporous Mater.*, 2006, **91**, 78–84.
- 30 V. M. Georgieva, E. L. Bruce, M. C. Verbraeken, A. R. Scott, W. J. Casteel, S. Brandani and P. A. Wright, *J. Am. Chem. Soc.*, 2019, **141**, 12744–12759.
- 31 P. Rzepka, D. Wardecki, S. Smeets, M. Müller, H. Gies, X. Zou and N. Hedin, *J. Phys. Chem. C*, 2018, **122**, 17211–17220.
- 32 (a) P. Nugent, Y. Belmabkhout, S. D. Burd, A. J. Cairns, R. Luebke, K. Forrest, T. Pham, S. Ma, B. Space, L. Wojtas, M. Eddaoudi and M. J. Zaworotko, *Nature*, 2013, **495**, 80–84; (b) Z. R. Herm, J. A. Swisher, B. Smit, R. Krishna and J. R. Long, *J. Am. Chem. Soc.*, 2011, **133**, 5664–5667.
- 33 R. Lin, L. Li, A. Alsalmeh and B. Chen, *Small Structures*, 2020, **1**, 2000022.
- 34 J. K. Bower, D. Barpaga, S. Proding, R. Krishna, H. T. Schaefer, B. P. McGrail, M. A. Derewinski and R. K. Motkuri, *ACS Appl. Mater. Interfaces*, 2018, **10**, 14287–14291.

